Journal of Materials Chemistry A

ROYAL SOCIETY OF CHEMISTRY

PAPER

View Article Online
View Journal | View Issue

Check for updates

Cite this: *J. Mater. Chem. A*, 2026, **14**, 7150

Mitigating structural deterioration *via* partial substitution with Fe in Mn-based Prussian white cathodes for Na-ion batteries

Adélaïde Clavelin,[abd] Marcus Fehse,[a] Moulay Tahar Sougrati,[cde] Carlos Escudero,[f] Lorenzo Stievano,[cde] Gabriel A. López,[b] Montserrat Galceran *[a] and Damien Saurel *[a]

Received 1st October 2025
Accepted 25th December 2025

DOI: 10.1039/d5ta08040a

rsc.li/materials-a

Prussian white (PW) is a promising cathode material for sodium-ion batteries (SIBs), which offers high theoretical capacity at low cost while being composed of abundant elements. However, Fe-based PW suffers from relatively low average voltage, and while substitution of one Fe with Mn can increase the voltage, it introduces structural instabilities supposedly due to the Jahn–Teller distortion of Mn^{3+}, resulting in poor capacity retention. In this work, we investigate the effect of partial substitution of Mn by Fe in Mn-based PW on electrochemical and structural stability. Two samples, $Na_{1.82}Mn[Fe(CN)_6]_{0.96}\cdot 2.0H_2O$ and $Na_{1.82}Mn_{0.62}Fe_{0.38}[Fe(CN)_6]_{0.96}\cdot 2.1H_2O$, were synthesized by coprecipitation and characterized *via* a multimodal approach combining laboratory and synchrotron-based techniques. We demonstrate that partial Mn substitution by Fe does not eliminate Jahn–Teller distortion but mitigates its negative effects by suppressing the distorted phase formation occurring near end of charge, thereby significantly enhancing capacity retention without sacrificing overall capacity. These results provide fundamental insight into the interplay between redox activity and structural stability in mixed-metal PW and establish partial Mn substitution by Fe as an effective strategy to improve long-term cyclability of PW cathodes for SIBs.

1 Introduction

The increasing demand for energy storage has led to a rise in the use of secondary batteries, raising concerns about the availability of several strategic and critical materials currently used in lithium-ion batteries (LIBs), the technology that dominates the energy storage landscape.[1] For this reason, interest in other M-ion technologies (M = Na, K, Ca, *etc.*), has increased over the last decade. Among these alternatives, sodium-ion batteries (SIBs) have gained the most interest thanks to their forecasted lower cost, partially due to higher availability of Na compared to Li and the possibility to use cheaper aluminum as the current collector instead of copper, and technological similarity to LIBs.[2–4]

Among the different cathode materials available for SIBs, Prussian Blue Analogues (PBAs) are an interesting candidate, due to their comparatively high theoretical capacity (*ca.* 170 mA h g^{-1}), low cost and high sustainability.[5–7] PBAs for SIBs have a general formula of $Na_{2-x}M_1[M_2(CN)_6]_{1-y}\cdot zH_2O$, with M_1 and M_2 being any transition metal. M_1 is usually in the high spin (HS) state as it is coordinated to the N-end of the CN ligands, while M_2 (mostly Fe) is coordinated to the C-end of the cyanide and usually in the low spin (LS) state. PBAs are historically called differently depending on their alkali ion content, that being Prussian white (PW) if the Na content is close to 2, and Berlin green (BG) if the Na content is close to 0. The most commonly studied PW materials for battery application are Fe-based, meaning M_1 and M_2 are both Fe, due to its low cost and high abundance. However, the energy density of these compounds remains lower than those of cathode materials for LIBs. A strategy to increase their energy density is to raise the average voltage, by replacing Fe with Mn in the M_1 site. Although this strategy was shown to increase the average voltage,[8] it is obtained at the expense of a reduced capacity retention, which is mainly attributed to Jahn–Teller distortion of Mn^{3+}.[9] To mitigate the poor performance while retaining high average voltage, several teams have studied the partial substitution of Mn by other transition metals. Among the most common alternative transition metals, Ni and Cu disqualify as

[a]*Center for Cooperative Research on Alternative Energies (CIC EnergiGUNE), Basque Research and Technology Alliance (BRTA), Parque Tecnológico de Alava, Albert Einstein 48, 01510, Vitoria-Gasteiz, Spain. E-mail: mgalceran@cicenergigune.com; dsaurel@cicenergigune.com*

[b]*Department of Physics, Faculty of Science and Technology, University of the Basque Country (UPV/EHU), Barrio Sarriena s/n, Leioa, Bilbao 48490, Spain*

[c]*ICGM, Univ. Montpellier, CNRS, Montpellier, France*

[d]*ALISTORE-European Research Institute, CNRS FR 3104, Hub de l'Energie, Rue Baudelocque, 80039 Amiens Cedex, France*

[e]*RS2E, CNRS, Amiens, France*

[f]*ALBA Synchrotron Light Source, Cerdanyola del Vallès, Barcelona 08290, Spain*

they are redox inactive within the stability voltage window of the CN network,[8,10] Co ore mining is ethically problematic and expensive, but promising results have been previously obtained when partially substituting Mn by Fe, in Na-ion or other M-ion technologies.[11–16] Despite this research interest, an in-depth analysis of the mechanism of this type of mixed composition PW for SIBs is still missing and, in particular, the impact of partial Mn substitution by Fe on electrochemical behaviour, capacity retention and structural stability remains unclear.

Therefore, this work aims to deepen the knowledge about redox and structural mechanisms of Mn–Fe mixed samples in SIBs. For this purpose, a sample without Mn substitution at the M_1 site ($Na_{1.82}Mn[Fe(CN)_6]_{0.96}\cdot 2.0H_2O$) and a sample with partial Mn substitution by Fe at the M_1 site ($Na_{1.82}Mn_{0.62}Fe_{0.38}[Fe(CN)_6]_{0.96}\cdot 2.1H_2O$) were synthesized by coprecipitation method. Material properties of both pristine materials were thoroughly investigated and differences in electrochemical behaviour and performance were highlighted. Their reaction mechanism was elucidated by combining complementary *operando* diffraction and spectroscopic techniques to monitor the crystal and electronic structure evolution upon the desodiation/sodiation reaction.

2 Experimental section

2.1. Materials synthesis

A coprecipitation method was used to synthesize the two samples, adapted from previous studies,[17–19] denoted as Mn-PW (no substitution at the M_1 site) and MnFe-PW (partial substitution of Mn by Fe at the M_1 site). Firstly, sodium ferrocyanide salt, $Na_4Fe(CN)_6$, was obtained by vacuum drying sodium ferrocyanide decahydrate ($Na_4Fe(CN)_6.10H_2O$, Sigma-Aldrich, 98%) overnight at 120 °C. Two solutions were then prepared: (1) solution A in a two-neck round-bottom flask containing 3 mmol of $Na_4Fe(CN)_6$ and 14 g of sodium chloride (NaCl, Sigma-Aldrich, 99%) in 25 mL ethanol and 75 mL water and (2) solution B containing 6 mmol of $MnSO_4.H_2O$ (Mn-PW) or 3 mmol of $MnSO_4.H_2O$ and 3 mmol of $FeSO_4.H_2O$ (MnFe-PW), in 100 mL water, with 15 g of sodium citrate dihydrate ($Na_3C_6H_5O_7.2H_2O$, Sigma-Aldrich, 99%) added as a chelating agent. The use of a water–ethanol mixture as the solvent has previously been shown to decrease the reaction rate.[20] A programmable pump was used to slowly transfer the solution (B) at 1 mL min^{-1} into the round-bottom flask containing solution A where the reaction occurred. The suspension was aged for 20 h without stirring to allow for decantation. The final products were washed and collected through centrifugation, before being dried under vacuum for 20 h at 120 °C.

2.2. Characterization methods

Quasi-simultaneous synchrotron X-ray diffraction (SXRD) at 13 keV photon energy ($\lambda = 0.95372$ Å) and X-ray absorption (XAS) measurements (Fe and Mn K-edges) were conducted at the NOTOS beamline[21] of the ALBA Synchrotron facility. X-ray Absorption Near Edge Structure (XANES) spectra were collected between 6500 and 6600 eV around the Mn K-edge and between 7100 and 7200 eV around the Fe K-edge. Extended X-ray Absorption Fine Structure (EXAFS) spectra for Mn and Fe were acquired up to $k = 12$ and 16.7 $Å^{-1}$, respectively. The beam spot was around 0.2 mm^2 and was monochromatized using a Si (111) double crystal, and harmonic rejection was performed using a collimating silicon mirror at 2.2 mrad. All XAS spectra were collected in transmission mode employing ion chambers filled with the appropriate mixture of inert gases to absorb around 15% of the photons in the ion chamber before the sample, and around 80% in the ion chamber after the sample and after the reference. An iron foil reference was measured at the same time to ensure the energy calibration during the XAS experiments. The EXAFS spectra were treated using Athena and fitted with Artemis software, both part of the DEMETER package.[22] The XRD patterns were refined by the Rietveld method using the FullProf software.[23] *Ex situ* electrodes at various states of charge (SOC), as well as a discharged electrode after 20 cycles, were measured at the NOTOS beamline, enabling quasi-simultaneous measurements of high quality XRD patterns and XAS spectra. The electrodes were sealed in plastic pouch bags, containing up to 16 electrodes each. The measurement of the two XAS edges and an XRD pattern required *ca.* 15 minutes per electrode. The structural integrity during the *ex situ* acquisition, most notably against rehydration, was confirmed by superimposing diffraction patterns at the beginning and end of the acquisition protocol, as shown in Fig. S1.

Scanning Electron Microscopy (SEM) images were obtained using a Quanta 200 FEG (FEI). The operating voltage and beam current were 20 kV and 1 nA, respectively. Samples for SEM were prepared by depositing some powder onto a carbon tape substrate glued onto an aluminum pin-holder for the electrons to be conducted and drained.

Transmission ^{57}Fe Mössbauer spectra were collected at room temperature with a triangular velocity waveform. A gas-filled counter was used for the detection of γ-rays. A 0.5 GBq ^{57}Co:Rh source was used. Velocity calibration was performed with an α-Fe foil standard at room temperature. The Mössbauer spectra were fitted by using the PC-Mos II computer program with appropriate superpositions of Lorentzian lines. To analyze the full *operando* Mössbauer dataset, a chemometric approach based on principal component analysis (PCA) and multivariate curve resolution-alternating least squares (MCR-ALS) analysis, described in detail elsewhere,[24] was used. The MCR-ALS analysis was performed with several constraints: (1) non-negativity of the intensity of the components, (2) closure (the sum of all components always equal to 100% of the intensity) and (3) a single starting component. The pure Mössbauer spectral components obtained from MCR-ALS analysis were then fitted as conventional Mössbauer spectra.

The amount of Na, Mn, Fe, C, H, N, and O in the targeted compositions was determined through inductively coupled plasma atomic emission spectroscopy (ICP-AES) and elemental analysis (EA) measurements, respectively. For the ICP measurements, the sample was digested in nitric acid using an ETHOS Easy (MILESTONE) microwave oven. The digested samples were characterized in a 7900 ICP-MS (Agilent Technologies) spectrometer while the EA was performed on a FlashSmart Elemental Analyser (Thermo Fisher Scientific).

Operando XRD measurements were performed on a lab-scale XRD instrument (Bruker D8 Advance and Malvern Panalytical Empyrean I) equipped with Cu Kα radiation ($\lambda_{CuK\alpha1} = 1.54056$ Å, $\lambda_{CuK\alpha2} = 1.5443$ Å), working in the Bragg–Brentano reflection geometry. *Operando* patterns were refined by the profile matching method using the FullProf App package.[25]

2.3. Electrochemical testing

For the standard electrochemical testing, electrodes were prepared by tape casting onto an aluminum current collector using a Dr Blade with a thickness of 0.25 mm of a slurry containing the active material (PW), conductive additive (carbon C65) and binder (polyvinylidene difluoride, PVDF) with a mass ratio of 70%:20%:10%, mixed homogeneously in 1-methyl-2-pyrrolidinone (NMP) solvent. The cast foil was then dried under vacuum at 80 °C overnight. Afterwards, disc electrodes of 12 mm diameter were punched and pressed under 2 tons by using a hydraulic press. Prior to cell assembly, the electrodes were dried for 20 h in a Buchi oven at 80 °C and under a vacuum of 20 mbar. This drying temperature has been chosen to only allow the removal of surface water, while interstitial and bound water is expected to still be present in the structure.[17]

Electrochemical performance at C/10 was investigated with 3-electrode Swagelok cells, composed of a PW working electrode and metallic sodium both as the counter and reference electrodes, respectively. Electrochemical performance at 1C was investigated in coin cells, composed of a PW working electrode and metallic sodium as the counter electrode. In all cells, 1 M $NaPF_6$ in 1 : 1 ethylene carbonate (EC): propylene carbonate (PC) electrolyte and Whatman glass-fiber separators were used. All cells were assembled in an Argon-filled glovebox. The cells were galvanostatically cycled at room temperature and a current density of C/10 or 1C between 2.0 V and 4.0 V *versus* Na^+/Na, where 1C corresponds to the capacity of 2 Na^+ exchanged per f.u., corresponding to a theoretical capacity of 171 mA h g^{-1} for the ideal materials.

For the *operando* analyses, the electrodes were prepared by mixing PW with C65 carbon and dry PTFE (poly(-tetrafluoroethylene)) at a weight ratio of 45% : 45% : 10% to produce a "self-standing" electrode. The *operando* experiments were carried out using a special electrochemical cell equipped with a Be window.[26] A piece of Al foil (thickness 8 micrometers for the XRD to maximize transmission) was placed between the working electrode and the Be window and used as the positive current collector. To obtain a good signal-to-noise ratio, the mass loadings of the active material of the self-standing electrodes were between 8 and 12 mg cm^{-2} for the *operando* XRD experiments and *ca.* 20 mg cm^{-2} for *operando* Mössbauer spectroscopy.

3 Results and discussion

3.1. Structure and chemical composition

The Rietveld refinements of the synchrotron XRD patterns of the Mn-PW and MnFe-PW samples, as shown in Fig. 1a and c, confirm that both compounds crystallize in the monoclinic system with the $P2_1/n$ space group, as expected for non-dried powder,[17] and exhibit no detectable secondary phases. The unit cell parameters determined from these Rietveld refinements (see Fig. 1a, c, Tables S1 and S2), are in agreement with those in previous studies.[18] The reflections observed between 16 and 19° are correlated with light-scattering atoms such as oxygen, carbon and nitrogen, and hence can be indicative of water content and its positions (see simulations in Fig. S2a). Both Mn-PW and MnFe-PW compounds show similar peak distributions in this area (see Fig. S2b), highlighting that the Mn-substitution does not significantly impact the water content or its distribution within the structure.

Both samples exhibit cuboid morphologies, as observed in the SEM images (see Fig. S3), as expected following a citrate-assisted synthesis protocol.[19] Additionally, to elucidate the oxidation state of iron in the synthesized materials, room temperature ^{57}Fe Mössbauer spectra were measured on the pristine samples (Fig. 1b and d). The Mössbauer spectrum of Mn-PW exhibits a sole unresolved doublet corresponding to LS Fe^{2+}, with no evidence of any iron oxidation (Table S3). In addition to the doublet of LS Fe^{2+}, the spectrum of MnFe-PW reveals the presence of HS Fe, confirming the successful substitution of Mn by Fe at the M_1 (HS) site. The spectrum can be fitted with three quadrupole doublets: an unresolved doublet (LS Fe^{2+}) and two resolved ones, corresponding to HS Fe^{2+} and HS Fe^{3+} (See Table S3). Although the HS Fe^{3+} component only represents around 3% of the total spectral area, this small fraction is sufficient to explain the blue color observed for the sample after the washing step (see Fig. S4).[27,28] Combining Mössbauer data, ICP and EA analyses (see Table S4) and refined Na-site occupancies, the approximate compositions of the two samples were determined as $Na_{1.82}Mn[Fe(CN)_6]_{0.96}\cdot 2.0H_2O$ for Mn-PW and $Na_{1.82}Mn_{0.62}Fe_{0.38}[Fe(CN)_6]_{0.96}\cdot 2.1H_2O$ for MnFe-PW. Notably, the ratio of HS Mn/HS Fe deviates from the stoichiometric ratio used in the precursor solution. This discrepancy may be attributed to (1) an excess of Mn/Fe precursor solution and (2) the difference of binding energy between sodium citrate and different metals, hence releasing the metal ions Mn^{2+} and Fe^{2+} at different rates. Such a phenomenon has been previously reported for Ni-based substitutions.[29]

3.2. Electrochemical results

The electrochemical profiles of the two studied materials, as well as their corresponding dQ/dV plots are presented in Fig. 2a. First-cycle discharge capacities of 133.8 mA h g^{-1} for Mn-PW and 120 mA h g^{-1} for MnFe-PW were obtained, corresponding to 85 and 76% of the maximum theoretical capacity available (*ca.* 157 mA h g^{-1} for both samples prior to drying), respectively, in line with the expected capacities for a hydrated phase.[11,18,30] Mn-PW shows the typical two-plateau profile of the hydrated monoclinic phase,[18] with a first plateau at around 3.4 V *vs.* Na^+/Na corresponding to the Fe^{2+}/Fe^{3+} redox reaction and a second plateau at around 3.8 V *vs.* Na^+/Na corresponding to the Mn^{2+}/Mn^{3+} redox reaction.[30,31] On the other hand, MnFe-PW shows three plateaus on charge, at 3.0, 3.4 and 3.8 V *vs.* Na^+/Na. Mn-PW exhibits an average voltage of 3.62 V *vs.* Na^+/Na in charge

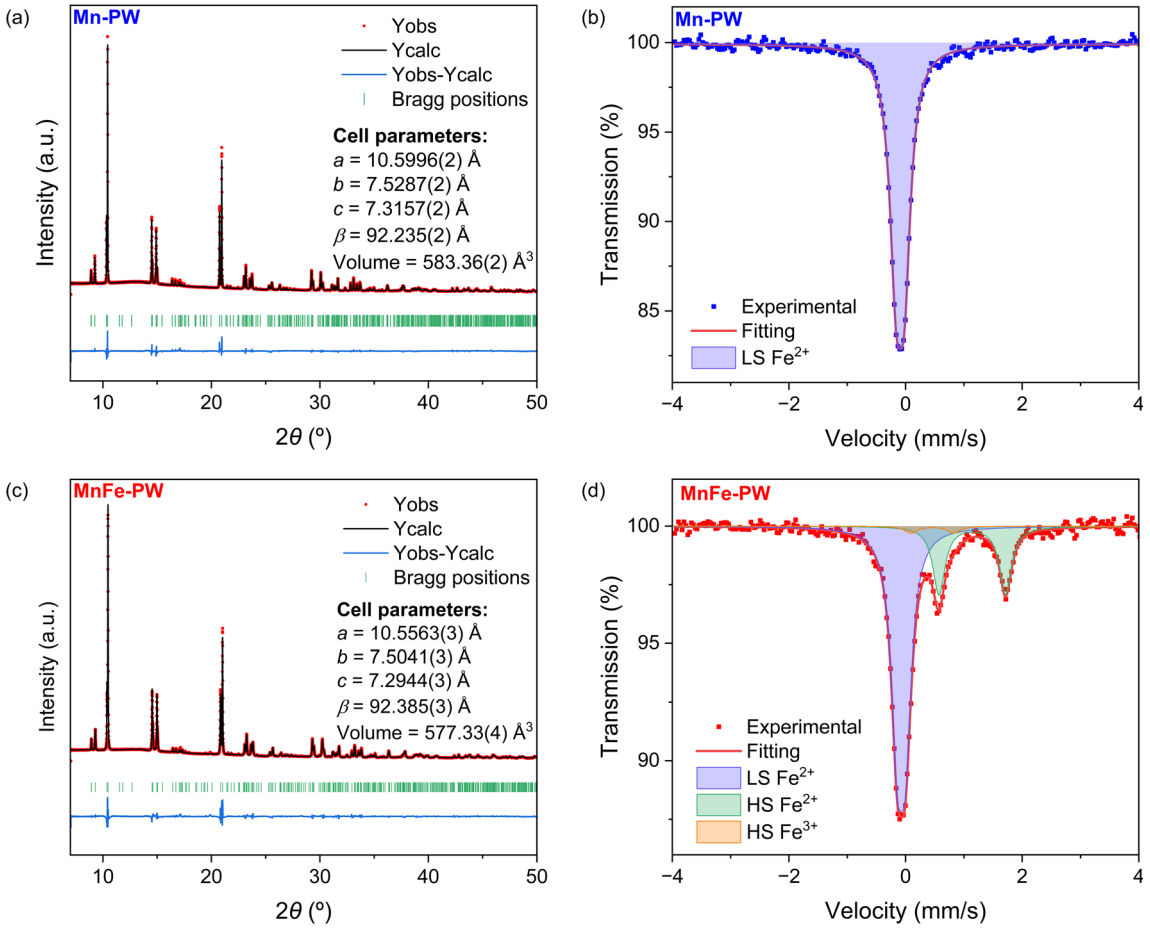

Fig. 1 Rietveld refinements of (a) Mn-PW and (c) MnFe-PW (λ = 0.95373 Å), with red dots showing observed data, the black line showing the calculated pattern, the blue line showing the difference between observed and calculated patterns and the vertical green bars showing the expected positions of Bragg reflections, and ^{57}Fe Mössbauer fittings of (b) Mn-PW and (d) MnFe-PW.

and of 3.34 V *vs.* Na+/Na in discharge, while MnFe-PW exhibits averages of 3.55 V *vs.* Na^+/Na and 3.26 V *vs.* Na^+/Na in charge and discharge, respectively. In comparison, Rudola *et al.*[32] reported an average discharge voltage of 3.03 V for monoclinic Fe-based PBA, cycling between 2 and 3.9 V. Other studies with Fe-based PBA report electrochemical reactions taking place mainly below 3.2 V in discharge.[32,33] Hence, both Mn-PW and MnFe-PW exhibit an increased average voltage compared to Fe-based PBAs.

The different electrochemical profiles of the two compounds suggest different sodiation reaction mechanisms, which could be related to a different succession of redox processes related to the substitution of Mn by Fe as well as differences in the structural phase transition sequences. In the following cycles, the electrochemical curve evolves for both samples, as shown in Fig. S5. The voltage steps between plateaus become smoother and the plateaus begin to merge, as previously observed in Mn-based PW and attributed to the *in situ* electrochemical dehydration of the material.[18,34] Hence, this gradual change of the profile could suggest partial dehydration of the sample during cycling.

To elucidate the reversibility and stability of the sodiation mechanism of the two materials, capacity retention tests were carried out and retained discharge capacity in per cent for each cycle, and the coulombic efficiency (CE) are shown in Fig. 2b. A salient difference in cycling stability is observed after 50 cycles at C/10: the partially substituted MnFe-PW shows a much higher capacity retention of about 93% compared to pure Mn-PW, which retains 62% of the initial discharge capacity. MnFe-PW also shows a higher coulombic efficiency compared to Mn-PW. Additional data at 1C (following 3 cycles at C/10) are shown in Fig. 2c, showing that the trends in capacity retention and coulombic efficiency observed at C/10 are also observed at higher C-rates. The low capacity retention of Mn-PW could be linked to the reduced reversibility of the charge/discharge process, and the observed differences in electrochemical cycling behaviour and cycling stability call for deeper mechanistic investigation.

3.3. Structural mechanistic study

The *operando* XRD patterns collected during cycling using a laboratory diffractometer (see Experimental section) for Mn-

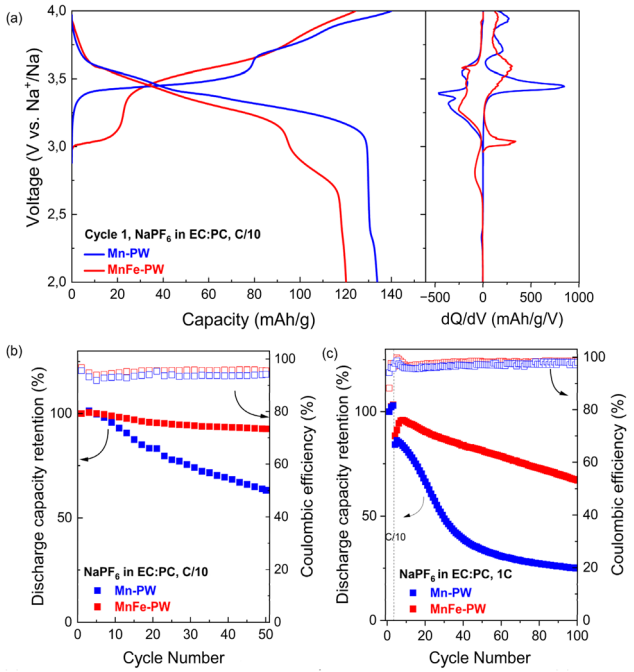

Fig. 2 (a) Electrochemical profile and corresponding dQ/dV plots of Mn-PW and MnFe-PW, (b) percentual discharge capacity retention and coulombic efficiency during the first 50 cycles at C/10 and (c) percentual discharge capacity retention and coulombic efficiency during the first 3 cycles at C/10 and the following cycles at 1C.

PW are shown in Fig. 3. A clear two-phase transition from a monoclinic to a cubic phase can be observed at the beginning of the first plateau, in agreement with recently published results.[35] When approaching the end of charge (EOC), two peaks at 17.4° and 24.2° appear while the intensity of the two nearby $(200)_C$ and $(220)_C$ reflections corresponding to the cubic phase decreases, indicating the occurrence of a second two-phase transition toward a new phase, which will be called C′ hereafter. This could be evidence of a tetragonal phase, appearing as a consequence of the Jahn–Teller distortion of Mn^{3+}, as reported before for similar compounds.[36–38] However, due to the limited resolution and 2θ range of the XRD patterns, it is not possible to perform quality Rietveld refinements at this stage, and therefore to confirm whether this new phase observed at the end of charge is actually a tetragonal phase. At the completion of the first discharge, the monoclinic phase is recovered, as seen by the splitting of the cubic peak $(220)_C$ at around 24°. However, the initial cell parameters are not fully recovered, as the initial peaks associated with $(200)_M$ and $(011)_M$ around 16.8°, and their second order $(400)_M$ and $(022)_M$ around 34°, appear merged at the end of the first cycle (see Fig. S6a), while they were clearly separated in the initial pattern (Fig. S6a). The capacity obtained at the end of the first discharge (111 mA h g^{-1}) is smaller than what has been observed in the Swagelok cell, which can be explained by differences in the cell configuration and higher loading optimized for XRD pattern acquisition rather than performance.[26] This is likely to influence overpotential and capacity but not the reaction pathways.

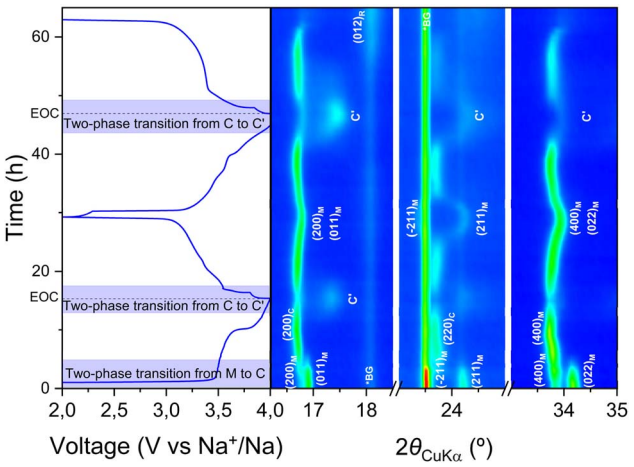

Fig. 3 *Operando* lab-XRD measurement of Mn-PW in the angular range of 16–35° ($2\theta_{CuK\alpha}$) (M = monoclinic, C = cubic, C′ = distorted cubic, R = rhombohedral, and *BG = background).

As the second cycle exhibits distinct behaviour compared to the first cycle, *vide supra*, the cell mechanism was followed during two cycles. It can be observed that at the end of the second discharge, the material undergoes a third transition to the rhombohedral phase, highlighted by the growth of the $(012)_R$ peak at 18.1°, overlapping with the background peak originating from the PTFE binder. The rhombohedral phase is typically obtained in Mn-based hexacyanoferrates by removing the interstitial and crystal water from the material,[17,18,35] hence suggesting that water is released from the structure upon cycling, therefore electrochemically "dewatering" the compound. This is consistent with the changes in the electrochemical profile observed earlier (*vide supra*).

Similar experiments were performed for MnFe-PW, as shown in Fig. 4. The *operando* XRD experiment reveals that, as Mn-PW, MnFe-PW undergoes a transition from monoclinic to cubic upon desodiation, however following a single phase transformation route. Moreover, towards the end of the charge

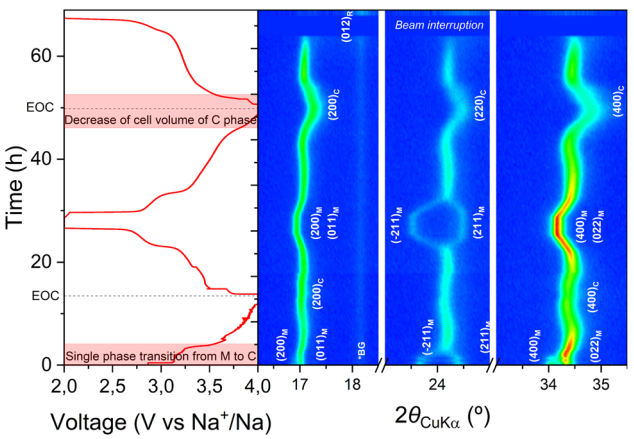

Fig. 4 *Operando* lab-XRD measurement of MnFe-PW in the angular range of 16–35° ($2\theta_{CuK\alpha}$) (M = monoclinic, C = cubic, R = rhombohedral, and *BG = background).

reaction, the material remains cubic, and no additional phase is observed. At the end of the first discharge, similar to Mn-PW, the monoclinic phase is recovered, although with a merging of the peaks $(011)_M/(200)_M$ and their second order (see Fig. S6b). During the second cycle, the cubic peaks shift to higher 2θ angles, suggesting a decrease in the unit cell volume. As for the Mn-PW sample, limited capacity is obtained during the first cycle. Due to beam interruption, the last patterns of the second discharge cycle could not be acquired under *operando* conditions. A final XRD pattern was hence acquired at the end of discharge (See Fig. S6b), which clearly depicts the coexistence of monoclinic and rhombohedral phases as for Mn-PW.

To complement the *operando* XRD analysis of the phase evolution, synchrotron derived *ex situ* XRD patterns were acquired at selected SOC (see Fig. 5 and 6) to provide deeper structural insights and were refined *via* the Rietveld method (Fig. S7, S8 and Tables S5–S12). As for the *operando* XRD experiment, the *ex situ* XRD patterns confirm that Mn-PW undergoes a transition from monoclinic to cubic to a new phase (C′) near the end of charge. The high-quality data allow us to clearly distinguish three different peaks in the region 10–11°, the main cubic peak $(200)_C$ and two peaks corresponding to the new phase C′, confirming that this new phase is not cubic. A first refinement of the *ex situ* SXRD pattern of Mn-PW at $x = 0.26$ using the tetragonal phase was performed, and the cell parameters obtained are $a = b = 7.1745(8)$Å and $c = 10.557(2)$ Å, similar to previously reported results.[36] As reported by two different groups,[36,39] the ratio $a/c = 0.680$ is lower than the ideal value of 0.707 which would be expected from the transformation of a face centered cubic to a body-centered tetragonal. Due to this deviation from the ideal value, it was previously suggested that this phase is actually not tetragonal but a monoclinic phase with a β angle close to 90°.[39] However, the Rietveld refinement of the *ex situ* SXRD pattern of Mn-PW at $x = 0.26$ with the monoclinic phase does not definitively confirm whether this distorted phase C′ at EOC is actually a tetragonal or a monoclinic phase, as both provide similar fit quality (see Fig. S7b and S9). In both cases, whether it being

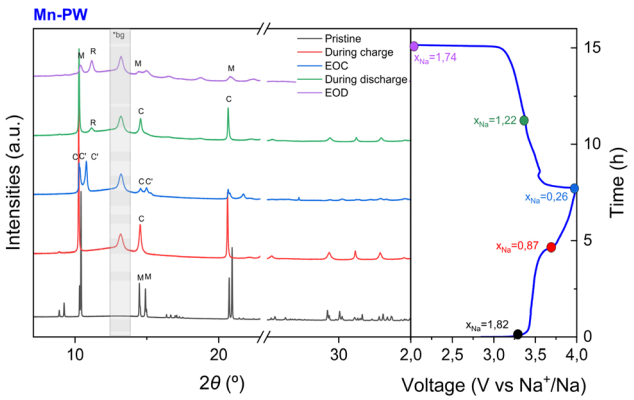

Fig. 5 *Ex situ* SXRD measurement of Mn-PW and first charge–discharge curve (M = monoclinic, C = cubic, C′ = distorted cubic and R = rhombohedral; *bg within the grey area indicates background peaks).

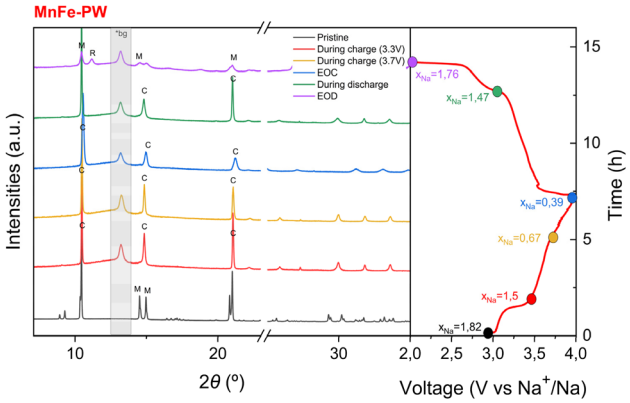

Fig. 6 *Ex situ* SXRD measurement of MnFe-PW and the first charge–discharge curve (M = monoclinic, C = cubic, and R = rhombohedral; *bg within the grey area indicates background peaks).

a distorted tetragonal phase or a monoclinic phase, this transformation from an ideal cubic structure to a distorted phase at EOC is consistent with the hypothesis of a Jahn–Teller effect. For clarity, this EOC phase will be referred to as a distorted cubic phase throughout the manuscript.

In the case of MnFe-PW, the *ex situ* SXRD patterns also confirm the observation made from the *operando* XRD of a transition from monoclinic to cubic at an early stage of charge, and then preserving the cubic phase until the end of the charge process with no transition toward a distorted phase near the end of charge. At the EOD, the *ex situ* SXRD patterns of both samples exhibit a mixture of monoclinic and rhombohedral phases. This is quite surprising, as in the *operando* XRD measurement discussed earlier, the rhombohedral phase appeared only during the second discharge. This is most likely due to the difference in the first discharge capacity between the *operando* and *ex situ* experiments, although an additional relaxation effect on the *ex situ* sample cannot be excluded. Interestingly, Mn-PW and MnFe-PW present different rhombohedral phase fractions at EOD, as Mn-PW contains a majority of the rhombohedral phase (53%), while MnFe-PW only contains 30%. This suggests that removal of water is more difficult in MnFe-PW than in Mn-PW, possibly due to the different evolution of the unit cell volume per formula unit during charge, as Mn-PW shows expansion of the lattice, which might facilitate the removal of water, while MnFe-PW shows the opposite trend (see Table S13).

Additionally, after 20 cycles, the discharged electrodes of both samples still exhibit a coexistence of monoclinic and rhombohedral phases, though with a higher relative amount of rhombohedral phase compared to the end of the first cycle (see Fig. S10), which indicates a continuous electrochemical dewatering of the crystal lattice upon cycling.

The refinements of *ex situ* SXRD measurements were used as a base to calculate the volume changes in both samples during charge from the *operando* data presented in Fig. 3 and 4, which are shown in Fig. 7. Interestingly, Mn-PW alternates between expansion of the lattice during the transition from monoclinic to cubic and shrinking of the lattice during the transformation

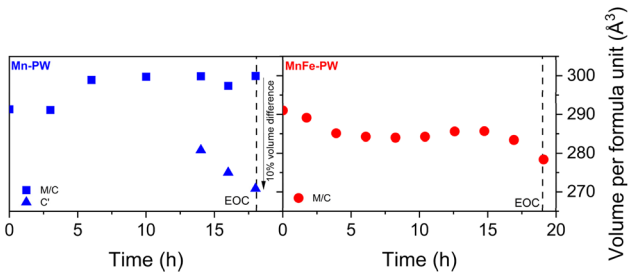

Fig. 7 Evolution of the volume per formula unit observed during the second cycle of the *operando* experiment for (left) Mn-PW and (right) MnFe-PW (M = monoclinic, C = cubic and C′ = distorted cubic).

from cubic into the distorted cubic phase. In particular, this later transition, near the end of charge, induces the coexistence of two phases with almost a 10% volumetric difference. This likely induces stress to the structure at the interfaces between the phases, which may accelerate the deterioration of the crystalline structure. The fact that this volumetric change, together with the appearance of the distorted cubic phase, occurs near the end of charge suggests that the $Mn^{2+} \rightarrow Mn^{3+}$ transition occurs only at that point rather than throughout the entire charging process, as this behaviour is likely related to the Jahn–Teller distortion at Mn^{3+}. In contrast, MnFe-PW does not undergo significant volume changes during the charging process, which is likely contributing to its improved cyclability. This is possibly related to the lower concentration of Mn^{3+} near the end of charge, as a consequence of the partial substitution of Mn by Fe compared to Mn-PW.

The formation of the distorted cubic phase is usually attributed to the collective Jahn–Teller distortion of the Mn^{3+} centres upon charge.[40] To determine if we observe a Jahn–Teller distortion during charge, the local structure of both samples was studied through EXAFS measurements, acquired quasi-simultaneously with the *ex situ* SXRD patterns previously described. Fitting details are provided in Table S14 and Fig. S11. The local structure of Mn undergoes severe distortion in both samples upon desodiation, shown mainly by the splitting of the first coordination shell (Mn–N) in two distinct shells, as shown in Fig. 8. This highlights the transition from an octahedral structure with 6 equi-distant Mn–N bonds to a distorted structure with two sets of bond lengths, in agreement with the occurrence of the Jahn–Teller effect. Interestingly, the coordination numbers of the two shells Mn–N(1) and Mn–N(2) are found to be 3 and 3 for both samples, hence deviating from the conventional Jahn–Teller distortion. It should be noted that a classical Jahn–Teller distortion (*i.e.* 4 compressed equatorial bonds and 2 elongated axial bonds) could only be achieved for MnFe-PW when different Debye–Waller parameters (varying by a factor up to 10) are permitted (see Table S15 and Fig. S12). For Mn-PW, attempts to fit with classical Jahn–Teller were unsuccessful. Such pseudo Jahn–Teller distortion has been previously observed for Li_xMnPO_4 battery materials.[41] In the case of PW materials, the presence of water in the structure and interstitial sites could possibly explain this deviation from the expected configuration. Indeed, it was previously observed that the removal of water strongly impacts the Mn K-edge in Mn-PW, showing that the presence of water plays a major role in the local environment of Mn and could therefore impact the accommodation of the distortion.[17]

Contrary to Mn, the local structure of the Fe absorber shows little variation upon charge for Mn-PW (see Fig. S13a), which is due to the strong π-acceptor properties of the cyanide ligand which lead the LS Fe (bonded to C) to retain its local environment. In detail, the first two shells, attributed to Fe–C and Fe–C–N bonds, remain unchanged during the cycling process. Merely small changes are observed at radial distances higher than 3 Å. For MnFe-PW on the other hand, stronger modifications of the local Fe environment are observed upon desodiation (see Fig. S13b). This is not unexpected since part of the Fe in this sample, bonded to the N-end of the cyanide, is in HS configuration. In this case, changes in the oxidation state strongly impact the local environment of HS Fe, compared to LS Fe,[11] and larger average variations are observed compared to Mn-PW.

The combination of long- and short-range structural analysis reveals strong local distortion around the Mn absorber in both

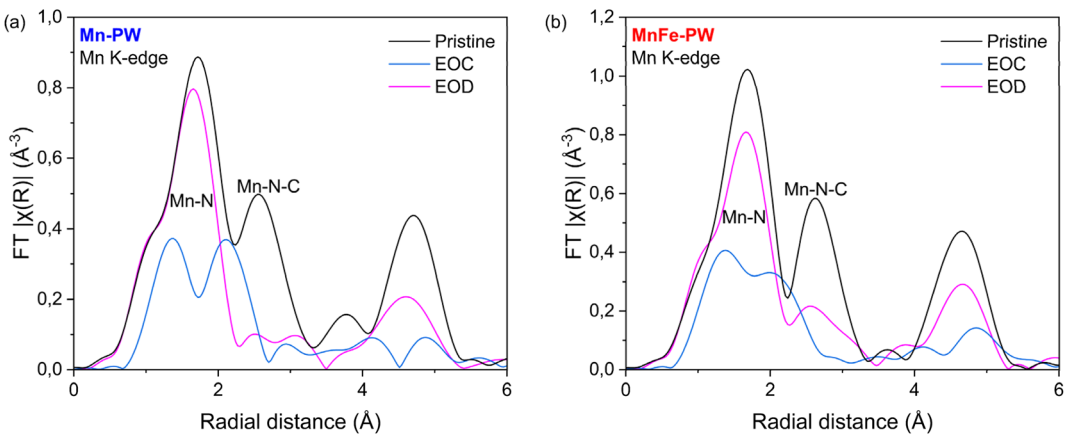

Fig. 8 FT EXAFS of the Mn K-edge for (a) Mn-PW and (b) MnFe-PW. Not phase shift corrected.

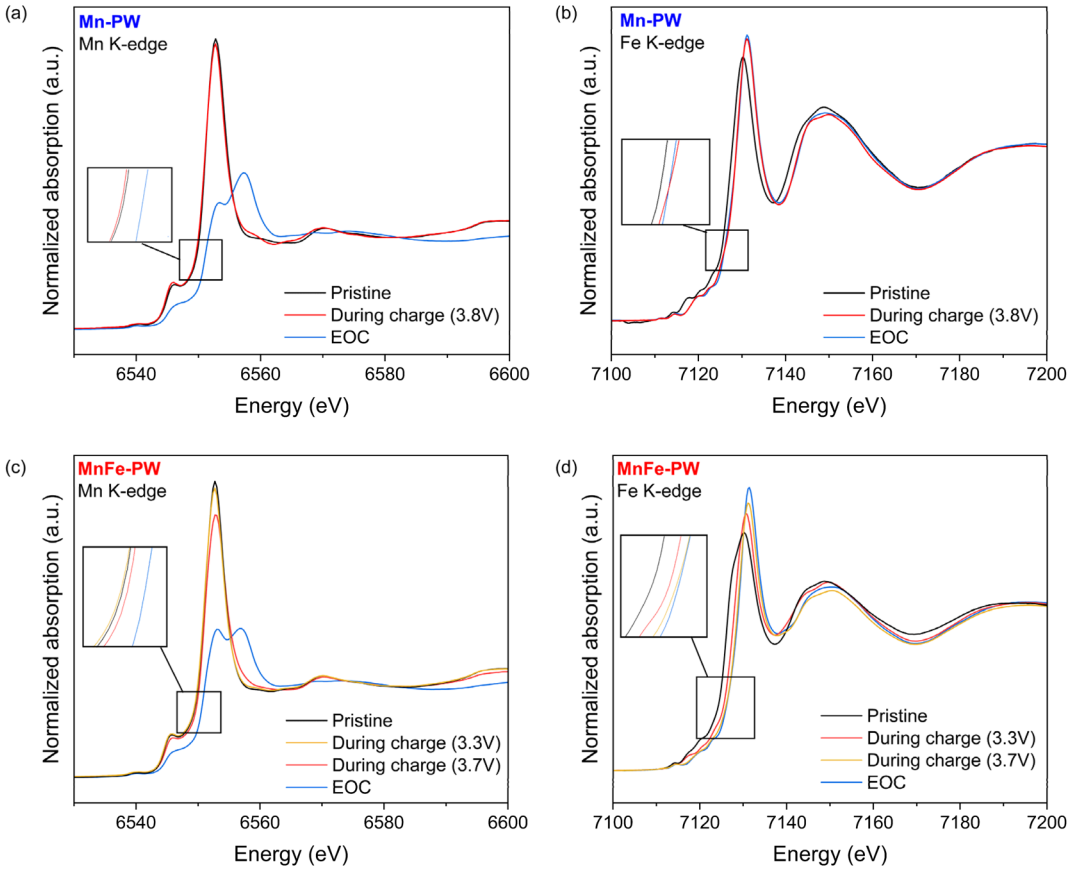

Fig. 9 XANES K-edge of *ex situ* samples at selected SOC for Mn-PW at (a) Mn and (b) Fe K-edges, and MnFe-PW at (c) Mn and (d) Fe K-edges.

samples, independent of the Mn content. However, in Mn-PW it appears that this pseudo Jahn–Teller effect results in stronger structural crystalline distortions than in mixed MnFe-PW, as evidenced by *operando* and *ex situ* XRD data. The partial substitution of Mn by Fe does not prevent the Jahn–Teller effect, but it seems to mitigate its detrimental impact on the structure, with the suppression of the transition to the distorted cubic phase in MnFe-PW, enabling enhanced structural stability and thereby improved cycle life.

3.4. Redox mechanistic study

To further investigate the observed difference in the redox reaction mechanism, Mössbauer spectroscopy and XAS were employed in a complementary manner. First, *ex situ* XAS spectra (Fig. 9) were acquired for both samples, along with the XRD patterns presented in Fig. 5 and 6. The Mn K-edge XANES spectra of Mn-PW remain unchanged along the first plateau and show an oxidative shift of the absorption edge only above 3.8 V. The EOC spectrum exhibits a strong change in edge shape, *i.e.*, a reduction of the white line intensity and the appearance of an additional peak at higher energy. This modification of the absorption edge is in line with the strong modification of the Mn local environment ascribed to the Jahn–Teller effect, as discussed in the previous section. Hence, the change in shape and shift between 3.8 V and EOC highlights the formation of Mn^{3+} Jahn–Teller active species in this voltage range, which is driving the previously observed transformation from the cubic to the distorted cubic phase. At EOC, the content of Mn^{3+} is estimated to be 45%, meaning that nearly one in two HS sites exhibits a Jahn–Teller distortion. The Fe K-edge XANES spectra (Fig. 9b) show a strong shift between OCV and 3.8 V, whereas only a minor shift and increase in the intensity of the white line are observed above this potential. These results are not surprising, as the shift of the absorption edge for LS Fe in hexacyanoferrate on going from Fe^{2+} to Fe^{3+} is known to be comparatively small in magnitude,[42,43] due to the strong π-acceptor properties of the cyanide ligand and the high covalency of the Fe–CN bonds (*vide supra*). From these results, the previously reported sequence of redox activity (*vide supra*) is confirmed: (1) the oxidation of Fe^{2+} to Fe^{3+} occurs during the low voltage plateau and (2) the oxidation of Mn^{2+} to Mn^{3+} during the high voltage plateau.

For MnFe-PW, no evident shift is observed in the Mn K-edge XANES spectra (Fig. 9c) before 3.7 V, suggesting that Mn^{2+} is mainly oxidized above 3.7 V, near the end of charge. At the EOC, a distortion of the Mn environment occurs, similar to Mn-PW, confirming the occurrence of the Jahn–Teller effect. The content of Mn^{3+} at EOC is estimated to be 41%, hence slightly less than in the case of Mn-PW. However, in this case, as the sample initially contains about 62% of Mn in the HS site, this means that about one in four HS sites exhibits a Jahn–Teller distortion, therefore close to two times less than in the case of

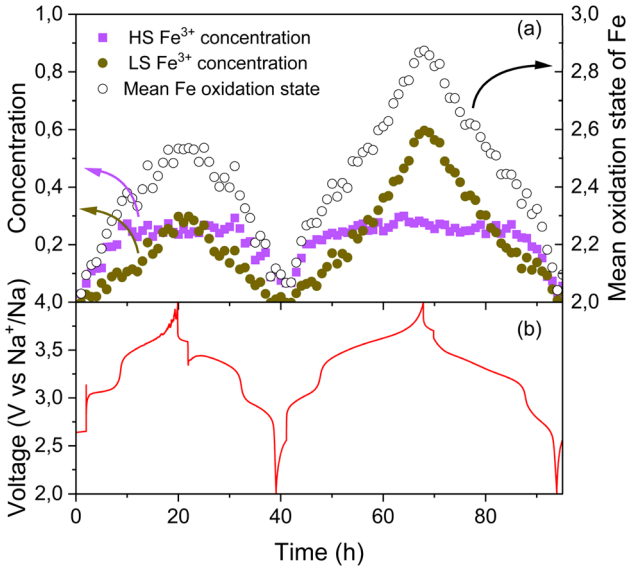

Fig. 10 (a) Evolution of the concentrations of LS and HS Fe^{3+} and of the mean oxidation state of Fe based on *operando* Mössbauer spectroscopy data and (b) the corresponding cycling curve of MnFe-PW.

Mn-PW. This is likely to contribute to less perturbation of the long-range structure. On the other hand, the Fe K-edge XANES spectra of MnFe-PW (Fig. 9d) show a salient shift from OCV up to 3.3 V, whereas only a minor shift is observed between 3.3 and 4 V (EOC). This confirms that the main redox activity of the HS Fe is occurring in the low voltage plateau. Moreover, as the edge shift upon oxidation of LS Fe^{2+} to LS Fe^{3+} is expected to be smaller compared to that of the HS configuration, the small shift observed above 3.3 V could correspond to the oxidation of LS Fe. Beyond 3.7 V, no major shift of the Fe is observed.

To further elucidate the contributions of LS and HS Fe in the electrochemical mechanism of MnFe-PW, *operando* Mössbauer spectra were acquired during two electrochemical cycles (Fig. S14). PCA applied on the full *operando* Mössbauer spectrum dataset (Fig. S15) indicates that three distinct spectral components are needed to describe the whole set of data. These components, reconstructed using the MCR-ALS algorithm, as well as the evolution of their relative concentration during cycling are shown in Fig. S16. The results of their fittings are shown in Fig. S17 and Table S16. Based on the fitted components and the computed concentrations shown in Fig. S16, the evolution of the LS and HS Fe can be monitored separately, along with the overall mean Fe oxidation state (Fig. 10a, solid and hollow markers, respectively).

This analysis reveals a clear spin state dependence of the iron redox activity. It is salient that HS Fe only reacts during the first plateau upon charge (until ~3.3 V) while LS Fe shows a continuous evolution during the entire desodiation process. LS iron redox shows a less steep slope implying slower kinetics than HS Fe. Based on these observations, the first plateau can be mainly ascribed to the reaction HS Fe^{2+} → HS Fe^{3+}, as previously reported for K-ion batteries.[11] Between 3.3 and 4 V, the concentration of LS Fe^{3+} is continuously evolving, while only a small shift of the absorption edge was observed between 3.7 and 4 V in the XANES spectra, owing to the high covalency of LS Fe in both oxidation states.

By combining the complementary insights from *operando* Mössbauer spectroscopy, *ex situ* XAS and *operando* XRD, a comprehensive picture of the sodiation mechanism can be established for Mn-PW and MnFe-PW which is summarized in Fig. 11a and b, respectively. For Mn-PW, the lower voltage plateau is attributed to the oxidation reaction Fe^{2+} → Fe^{3+}, during which a two-phase transition from monoclinic to cubic is occurring. The higher voltage plateau is attributed to the oxidation reaction Mn^{2+} → Mn^{3+}, inducing pronounced Jahn–Teller effects in nearly half of the HS sites, which drives the two-phase transition from cubic to the distorted cubic C′ phase. For MnFe-PW, the iron redox reaction is clearly subdivided. First, the oxidation of HS Fe^{2+} occurs up to 3.3 V, accompanied by

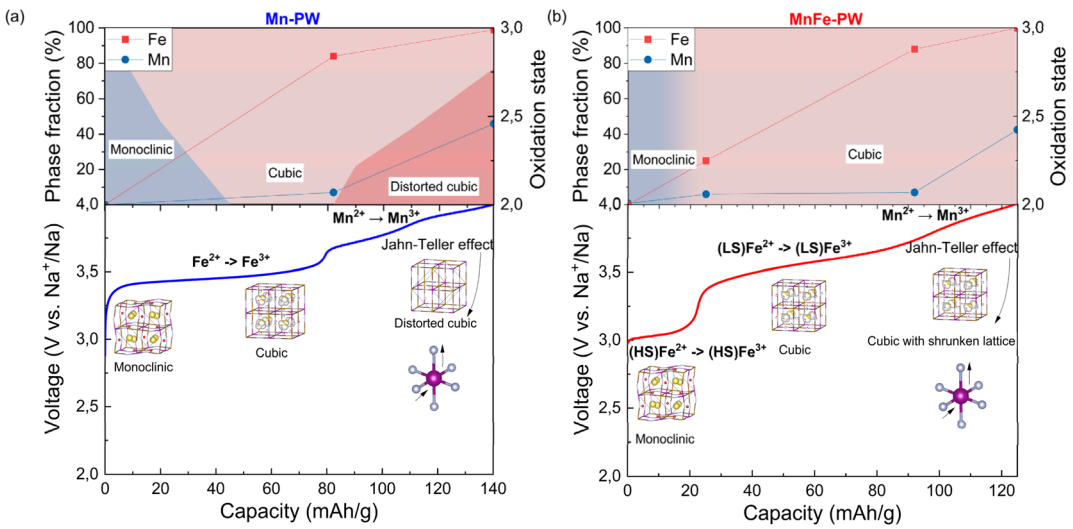

Fig. 11 Synchronized mapping of the different techniques used to unravel the complete sodiation mechanism for (a) Mn-PW and (b) MnFe-PW.

a single-phase transition from monoclinic to cubic, completed after the voltage jump. Beyond this voltage it is overtaken by the oxidation of LS Fe^{2+} which blends into the oxidation of Mn^{2+} taking over the main redox contribution above 3.7 V. The Mn oxidation occurs along with a decrease in the cubic unit cell volume. Analogous to Mn-PW, the formation of Mn^{3+} species during this highest reaction plateau induces a Jahn–Teller distortion. However, unlike Mn-PW, the partial substitution of Mn by Fe in MnFe-PW results in about twice less Jahn–Teller active HS sites, stabilizing the structure and mitigating its detrimental effect.

4 Conclusions

In this study, two different PW electrode materials were synthesized and investigated: one containing Mn at the N-coordinated site and another with partial substitution of Mn by Fe. The introduction of Fe at the Mn site was found to markedly improve capacity retention during prolonged cycling, while preserving the initial capacity. A multimodal characterization approach combining lab-scale and synchrotron-based techniques, with *operando* and *ex situ* analyses, revealed the occurrence of a Jahn–Teller distortion of Mn^{3+} in both materials. This distortion arises at the final stage of the charge process, in agreement with the established sequence of redox reactions. Although similar local distortions around Mn are observed in both Mn-PW and MnFe-PW, the latter exhibits a less pronounced impact on the long-range crystal structure, as evidenced by the suppression of the transition towards a distorted cubic phase involving detrimental lattice strain. The comprehensive structural and redox analysis clarifies the role of Mn-to-Fe substitution in SIBs, revealing it as an effective strategy to mitigate the Jahn–Teller induced distortions and thereby stabilize electrochemical cycling, while preserving the high initial performance of the material. Given the cycling stability improvement, further optimization of the Mn-to-Fe ratio is of high interest. The sample studied in this work offers a good compromise between high voltage due to Mn, and enhanced stability provided by the Fe. Increasing the Fe content would most likely result in lower average voltage, hence reducing the energy density of the cell and diminishing the advantage of using Mn. A slightly higher Mn content might be interesting, but the effects on cycling stability need further investigation.

Conflicts of interest

There are no conflicts of interest to declare.

Data availability

We certify that the data corresponding to the results reported in our paper "Mitigating structural deterioration *via* partial substitution with Fe in Mn-based Prussian white cathodes for Na-ion batteries" by Clavelin *et al.* will be available when asked, not only those mentioned in the manuscript but also in supplementary information (SI). Supplementary information is available. See DOI: https://doi.org/10.1039/d5ta08040a.

Acknowledgements

As a part of the DESTINY PhD Programme, this publication was supported by funding from the European Union's Horizon2020 Research and Innovation Programme under the Marie Skłodowska-Curie Actions COFUND (Grant Agreement # 945357). This publication is also part of the R&D project PID2022-140823OB-I00 funded by MICIU/AEI/10.13039/501100011033 and by EDRF A way of making Europe. Financial support by the Basque Goverment through the IT1714-22 project is also acknowledged. LS and MTS acknowledge funding from the French National Research Agency (Project Labex STORE-EX, ANR-10-LABX-76-01). These experiments were performed at the NOTOS beamline at ALBA Synchrotron (proposal 2024028266) with the collaboration of ALBA staff. The authors acknowledge Ivan Bobrikov and Bernard Fraisse for their support during the *operando* XRD acquisitions.

References

1 C. Xu, Q. Dai, L. Gaines, M. Hu, A. Tukker and B. Steubing, Future Material Demand for Automotive Lithium-Based Batteries, *Commun. Mater.*, 2020, **1**, 99, DOI: 10.1038/s43246-020-00095-x.
2 P. K. Nayak, L. Yang, W. Brehm and P. Adelhelm, From Lithium-Ion to Sodium-Ion Batteries: Advantages, Challenges, and Surprises, *Angew. Chem., Int. Ed.*, 2018, **57**, 102–120, DOI: 10.1002/anie.201703772.
3 K. M. Abraham, How Comparable Are Sodium-Ion Batteries to Lithium-Ion Counterparts?, *ACS Energy Lett.*, 2020, **5**, 3544–3547, DOI: 10.1021/acsenergylett.0c02181.
4 I. Hasa, S. Mariyappan, D. Saurel, P. Adelhelm, A. Y. Koposov, C. Masquelier, L. Croguennec and M. Casas-Cabanas, Challenges of Today for Na-Based Batteries of the Future: From Materials to Cell Metrics, *J. Power Sources*, 2021, **482**, 228872, DOI: 10.1016/j.jpowsour.2020.228872.
5 B. Wang, Y. Han, X. Wang, N. Bahlawane, H. Pan, M. Yan and Y. Jiang, Prussian Blue Analogs for Rechargeable Batteries, *iScience*, 2018, **3**, 110–133, DOI: 10.1016/j.isci.2018.04.008.
6 J. Qian, C. Wu, Y. Cao, Z. Ma, Y. Huang, X. Ai and H. Yang, Prussian Blue Cathode Materials for Sodium-Ion Batteries and Other Ion Batteries, *Adv. Energy Mater.*, 2018, **8**, 1702619, DOI: 10.1002/aenm.201702619.
7 Y. Xiao, J. Xiao, H. Zhao, J. Li, G. Zhang, D. Zhang, X. Guo, H. Gao, Y. Wang, J. Chen, G. Wang and H. Liu, Prussian Blue Analogues for Sodium-Ion Battery Cathodes: A Review of Mechanistic Insights, Current Challenges, and Future Pathways, *Small*, 2024, **20**, 2401957, DOI: 10.1002/smll.202401957.
8 X. Bie, K. Kubota, T. Hosaka, K. Chihara and S. Komaba, Synthesis and Electrochemical Properties of Na-Rich Prussian Blue Analogues Containing Mn, Fe, Co, and Fe for Na-Ion Batteries, *J. Power Sources*, 2018, **378**, 322–330, DOI: 10.1016/j.jpowsour.2017.12.052.
9 Y. Tang, W. Li, P. Feng, M. Zhou, K. Wang, Y. Wang, K. Zaghib and K. Jiang, High-Performance Manganese Hexacyanoferrate with Cubic Structure as Superior Cathode

Material for Sodium-Ion Batteries, *Adv. Funct. Mater.*, 2020, **30**, 1908754, DOI: 10.1002/adfm.201908754.

10 Y. You, X.-L. Wu, Y.-X. Yin and Y.-G. Guo, A Zero-Strain Insertion Cathode Material of Nickel Ferricyanide for Sodium-Ion Batteries, *J. Mater. Chem. A*, 2013, **1**, 14061, DOI: 10.1039/c3ta13223d.

11 P. N. Le Pham, R. Wernert, M. Cahu, M. T. Sougrati, G. Aquilanti, P. Johansson, L. Monconduit and L. Stievano, Prussian Blue Analogues for Potassium-Ion Batteries: Insights into the Electrochemical Mechanisms, *J. Mater. Chem. A*, 2023, **11**, 3091–3104, DOI: 10.1039/D2TA08439B.

12 Y. Moritomo, S. Urase and T. Shibata, Enhanced Battery Performance in Manganese Hexacyanoferrate by Partial Substitution, *Electrochim. Acta*, 2016, **210**, 963–969, DOI: 10.1016/j.electacta.2016.05.205.

13 Y. Xi and Y. Lu, Electrochemically Active Mn-Doped Iron Hexacyanoferrate as the Cathode Material in Sodium-Ion Batteries, *ACS Appl. Mater. Interfaces*, 2022, **14**, 39022–39030, DOI: 10.1021/acsami.2c07779.

14 G. Yang, Z. Liang, Q. Li, Y. Li, F. Tian and C. Wang, Epitaxial Core–Shell MnFe Prussian Blue Cathode for Highly Stable Aqueous Zinc Batteries, *ACS Energy Lett.*, 2023, **8**, 4085–4095, DOI: 10.1021/acsenergylett.3c01603.

15 W. Li, C. Han, W. Wang, Q. Xia, S. Chou, Q. Gu, B. Johannessen, H. Liu and S. Dou, Stress Distortion Restraint to Boost the Sodium Ion Storage Performance of a Novel Binary Hexacyanoferrate, *Adv. Energy Mater.*, 2019, **10**(4), DOI: 10.1002/aenm.201903006.

16 L. Jiang, Y. Lu, C. Zhao, L. Liu, J. Zhang, Q. Zhang, X. Shen, J. Zhao, X. Yu, H. Li, X. Huang, L. Chen and Y.-S. Hu, Building Aqueous K-Ion Batteries for Energy Storage, *Nat. Energy*, 2019, **4**, 495–503, DOI: 10.1038/s41560-019-0388-0.

17 A. Clavelin, D. L. Thanh, I. Bobrikov, M. Fehse, N. E. Drewett, G. A. López, D. Saurel and M. Galceran, Dehydration Conditions and Ultrafast Rehydration of Prussian White: Phase Transition Dynamics and Implications for Sodium-Ion Batteries, *ACS Mater. Lett.*, 2024, **6**, 5208–5214, DOI: 10.1021/acsmaterialslett.4c01833.

18 J. Song, L. Wang, Y. Lu, J. Liu, B. Guo, P. Xiao, J.-J. Lee, X.-Q. Yang, G. Henkelman and J. B. Goodenough, Removal of Interstitial H_2O in Hexacyanometallates for a Superior Cathode of a Sodium-Ion Battery, *J. Am. Chem. Soc.*, 2015, **137**, 2658–2664, DOI: 10.1021/ja512383b.

19 X. Wu, C. Wu, C. Wei, L. Hu, J. Qian, Y. Cao, X. Ai, J. Wang and H. Yang, Highly Crystallized $Na_2CoFe(CN)_6$ with Suppressed Lattice Defects as Superior Cathode Material for Sodium-Ion Batteries, *ACS Appl. Mater. Interfaces*, 2016, **8**, 5393–5399, DOI: 10.1021/acsami.5b12620.

20 J. Wang, Z. Wang, H. Liu, J. Gao, Y. Xu, Z. Chen, X. Li and Y. Liu, Synthesis of Fe-Doped Mn-Based Prussian Blue Hierarchical Architecture for High-Performance Sodium Ion Batteries, *Electrochim. Acta*, 2023, **448**, 142183, DOI: 10.1016/j.electacta.2023.142183.

21 C. Marini, C. Escudero, E. Villalobos–Portillo, I. Lucentini, J. Prat Albert, M. Armengol–Profitós, D. Heinis, O. Vallcorba, F. Fauth, A. P. Black, M. R. Palacin, J. B. González Fernández, A. Baucells, J. R. García Molinero, R. J. Homs, N. Serra, J. Nicolàs and G. Agostini, BL16 NOTOS, an X-Ray Absorption and Diffraction Beamline for Operando Battery Studies at ALBA, *Eur. Phys. J. Plus*, 2025, **140**, DOI: 10.1140/epjp/s13360-025-07170-7.

22 B. Ravel and M. Newville, ATHENA, ARTEMIS, HEPHAESTUS: Data Analysis for X-Ray Absorption Spectroscopy Using IFEFFIT, *J. Synchrotron Radiat.*, 2005, **12**, 537–541, DOI: 10.1107/s0909049505012719.

23 J. Rodríguez-Carvajal, Recent Advances in Magnetic Structure Determination by Neutron Powder Diffraction, *Phys. B*, 1993, **192**, 55–69, DOI: 10.1016/0921-4526(93)90108-I.

24 M. Fehse, A. Iadecola, M. T. Sougrati, P. Conti, M. Giorgetti and L. Stievano, Applying Chemometrics to Study Battery Materials: Towards the Comprehensive Analysis of Complex Operando Datasets, *Energy Storage Mater.*, 2019, **18**, 328–337, DOI: 10.1016/j.ensm.2019.02.002.

25 O. Arcelus, J. Rodríguez-Carvajal, N. A. Katcho, M. Reynaud, A. P. Black, D. Chatzogiannakis, C. Frontera, J. Serrano-Sevillano, M. Ismail, J. Carrasco, F. Fauth, M. R. Palacin and M. Casas-Cabanas, *FullProfAPP*: A Graphical User Interface for the Streamlined Automation of Powder Diffraction Data Analysis, *J. Appl. Crystallogr.*, 2024, **57**, 1676–1690, DOI: 10.1107/s1600576724006885.

26 D. Saurel, A. Pendashteh, M. Jáuregui, M. Reynaud, M. Fehse, M. Galceran and M. Casas-Cabanas, Experimental Considerations for *Operando* Metal-Ion Battery Monitoring Using X-ray Techniques, *Chem.:Methods*, 2021, **1**, 249–260, DOI: 10.1002/cmtd.202100009.

27 M. B. Robin, The Color and Electronic Configurations of Prussian Blue, *Inorg. Chem.*, 1962, **1**, 337–342, DOI: 10.1021/ic50002a028.

28 L. Samain, F. Grandjean, G. J. Long, P. Martinetto, P. Bordet and D. Strivay, Relationship between the Synthesis of Prussian Blue Pigments, Their Color, Physical Properties, and Their Behavior in Paint Layers, *J. Phys. Chem. C*, 2013, **117**, 9693–9712, DOI: 10.1021/jp3111327.

29 R. Chen, Y. Huang, M. Xie, Z. Wang, Y. Ye, L. Li and F. Wu, Chemical Inhibition Method to Synthesize Highly Crystalline Prussian Blue Analogs for Sodium-Ion Battery Cathodes, *ACS Appl. Mater. Interfaces*, 2016, **8**, 31669–31676, DOI: 10.1021/acsami.6b10884.

30 J. Sottmann, F. L. M. Bernal, K. V. Yusenko, M. Herrmann, H. Emerich, D. S. Wragg and S. Margadonna, In Operando Synchrotron XRD/XAS Investigation of Sodium Insertion into the Prussian Blue Analogue Cathode Material Na 1.32 Mn[Fe(CN) 6] 0.83 · z H 2 O, *Electrochim. Acta*, 2016, **200**, 305–313, DOI: 10.1016/j.electacta.2016.03.131.

31 T. Matsuda, M. Takachi and Y. Moritomo, A Sodium Manganese Ferrocyanide Thin Film for Na-Ion Batteries, *Chem. Commun.*, 2013, **49**, 2750, DOI: 10.1039/c3cc38839e.

32 Z. Li, S. Zhong, B. Zhou, D. Chen, Z. Qiu, R. Zhang, R. Zheng, C. Zhao and J. Zhou, Synthesis of Low-Defect Iron-Based Prussian Blue with Low Water Content for High-Stability Sodium-Ion Batteries, *Materials*, 2025, **18**, 1455, DOI: 10.3390/ma18071455.

33 P. S. Camacho, R. Wernert, M. Duttine, A. Wattiaux, A. Rudola, P. Balaya, F. Fauth, R. Berthelot, L. Monconduit, D. Carlier and L. Croguennec, Impact of Synthesis Conditions in Na-Rich Prussian Blue Analogues, *ACS Appl. Mater. Interfaces*, 2021, **13**, 42682–42692, DOI: 10.1021/acsami.1c09378.

34 J. Wu, J. Song, K. Dai, Z. Zhuo, L. A. Wray, G. Liu, Z. Shen, R. Zeng, Y. Lu and W. Yang, Modification of Transition-Metal Redox by Interstitial Water in Hexacyanometalate Electrodes for Sodium-Ion Batteries, *J. Am. Chem. Soc.*, 2017, **139**, 18358–18364, DOI: 10.1021/jacs.7b10460.

35 Z. Li, Y. Wang, F. Rabuel, M. Deschamps, G. Rousse, O. Sel and J.-M. Tarascon, Na2-Mn[Fe(CN)6] Prussian Blue Analog Cathodes for Na-Ion Batteries – From Fundamentals to Practical Demonstration, *Energy Storage Mater.*, 2025, **76**, 104118, DOI: 10.1016/j.ensm.2025.104118.

36 Y. Shang, X. Li, J. Song, S. Huang, Z. Yang, Z. J. Xu and H. Y. Yang, Unconventional Mn Vacancies in Mn–Fe Prussian Blue Analogs: Suppressing Jahn-Teller Distortion for Ultrastable Sodium Storage, *Chem*, 2020, **6**, 1804–1818, DOI: 10.1016/j.chempr.2020.05.004.

37 F. Gebert, D. L. Cortie, J. C. Bouwer, W. Wang, Z. Yan, S. Dou and S. Chou, Epitaxial Nickel Ferrocyanide Stabilizes Jahn–Teller Distortions of Manganese Ferrocyanide for Sodium-Ion Batteries, *Angew. Chem., Int. Ed.*, 2021, **60**, 18519–18526, DOI: 10.1002/anie.202106240.

38 L. Deng, J. Qu, X. Niu, J. Liu, J. Zhang, Y. Hong, M. Feng, J. Wang, M. Hu, L. Zeng, Q. Zhang, L. Guo and Y. Zhu, Defect-Free Potassium Manganese Hexacyanoferrate Cathode Material for High-Performance Potassium-Ion Batteries, *Nat. Commun.*, 2021, **12**, 2167, DOI: 10.1038/s41467-021-22499-0.

39 M. Li, M. Gaboardi, A. Mullaliu, M. Maisuradze, X. Xue, G. Aquilanti, J. Rikkert Plaisier, S. Passerini and M. Giorgetti, Influence of Vacancies in Manganese Hexacyanoferrate Cathode for Organic Na-Ion Batteries: A Structural Perspective, *ChemSusChem*, 2023, **16**, e202300201, DOI: 10.1002/cssc.202300201.

40 K. Ren, L. Chen, C. Liu, Y. Tian, X. Leng, M. Jiang, Z. Han, G. Xiao, G. Xu, Z. Yu, P. Wang, Y. Xie, Y. He and T. Yi, Ligand Field Electronic State Regulation of Monoclinic Prussian White Toward Highly Stable Sodium-Ion Batteries, *Adv. Mater.*, 2025, 2507960, DOI: 10.1002/adma.202507960.

41 L. F. J. Piper, N. F. Quackenbush, S. Sallis, D. O. Scanlon, G. W. Watson, K.-W. Nam, X.-Q. Yang, K. E. Smith, F. Omenya, N. A. Chernova and M. S. Whittingham, Elucidating the Nature of Pseudo Jahn–Teller Distortions in Li_xMnPO_4: Combining Density Functional Theory with Soft and Hard X-Ray Spectroscopy, *J. Phys. Chem. C*, 2013, **117**, 10383–10396, DOI: 10.1021/jp3122374.

42 P. A. Morozova, S. V. Ryazantsev, A. D. Dembitskiy, A. V. Morozov, G. Das, G. Aquilanti, M. Gaboardi, J. R. Plaisier, A. A. Tsirlin, I. A. Presniakov, A. M. Abakumov and S. S. Fedotov, Unexpected Chain of Redox Events in Co-Based Prussian Blue Analogues, *Chem. Mater.*, 2023, **35**, 3570–3581, DOI: 10.1021/acs.chemmater.3c00207.

43 A. Mullaliu, G. Aquilanti, P. Conti, J. R. Plaisier, M. Fehse, L. Stievano and M. Giorgetti, Copper Electroactivity in Prussian Blue-Based Cathode Disclosed by Operando XAS, *J. Phys. Chem. C*, 2018, **122**, 15868–15877, DOI: 10.1021/acs.jpcc.8b03429.